## **Supporting Information**

Maskless Micro/Nanopatterning and Bipolar Electrical-Rectification of MoS<sub>2</sub> Flakes Through Femtosecond Laser Direct Writing

Pei Zuo,¹ Lan Jiang,¹ Xin Li,\*,¹ Mengyao Tian,¹ Chenyang Xu,¹ Yongjiu Yuan,¹ Peng Ran,¹ Bo Li,¹ Yongfeng Lu²

<sup>1</sup>Laser Micro/Nano Fabrication Laboratory, School of Mechanical Engineering, Beijing Institute of Technology, Beijing 100081, P.R. China,

<sup>2</sup>Department of Electrical and Computer Engineering, University of Nebraska-Lincoln, Lincoln, NE 68588-0511, USA

<sup>\*</sup>Address correspondence to <a href="mailto:lixin02@bit.edu.cn">lixin02@bit.edu.cn</a>

#### Supplementary tables, figures and analysis.

Table S1 Laser processing parameters for MoS<sub>2</sub> micro/nanostructures as shown in Figure 2.

Number	Pulse energy (μJ)	Scan interval (µm)	Scan speed (µm/s)
Figure 2a	0.015	0.5	20
Figure 2b	0.015	0.5	10
Figure 2c	0.020	0.5	20
Figure 2d	0.020	0.5	5
Figure 2e	0.015	0.1	50
Figure 2f-1	ejecteo	d material of MoS <sub>2</sub> when	processed
Figure 2f-2	0.08		5
Figure 2g	0.040	every groove repeatedly processed 6 times	5
Figure 2h	0.080		5

The formation way of  $MoS_2$  micro/nanostructures and dependence of widths of nanoribbons on laser processing parameters (pulse energy and scan speed).

Conventional laser direct writing. The method of conventional laser direct writing is to remove or modify material at where laser spot scans (schematic is showed in Figure S1). In fact, processing method based conventional laser direct writing was also used in the work, the results are show as Figure 2g, Figure 2h, and image (below) in Figure 2f.

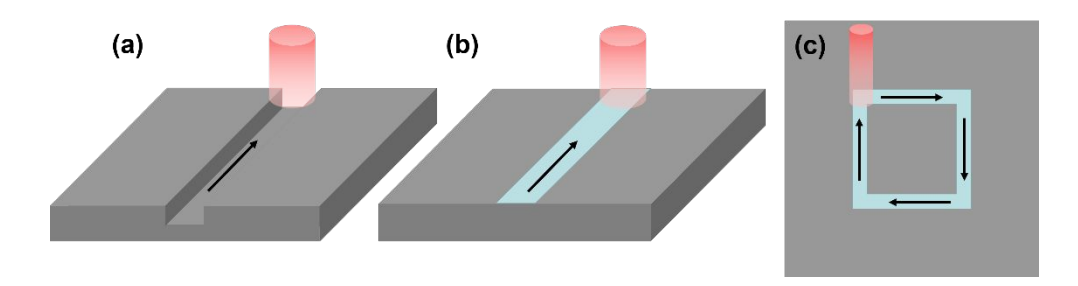


Figure S1. Method of conventional laser direct writing for (a) material removal, (b) surface modification, and (c) patterning.

Formation of MoS<sub>2</sub> nanostructures (nanoribbons) shown in Figure 2a-e. The formation of MoS<sub>2</sub> nanostructures (nanoribbons with different widths) was based on the formation of regular nanostructures (1aser-induced periodic surface structure, LIPSS/ripple) and material removal induced by femtosecond laser irradiation. These LIPSS/ripples are surface micro/nano structures for bulk material with big thickness. About the depth of gaps of laser induced grating structures of MoS<sub>2</sub>:

There are literatures stating that depth of gaps (caused by material removal) between laser-induced grating structures is influenced by the number and energy of ultrafast laser pulses on unit area of material, and can be on a micrometer scale. S1-3 The MoS<sub>2</sub> used in our experiment was nano-scale thin (several to dozens of nanometers) flakes, therefore controlling appropriate pulse energy and scan speed of laser beam can control the gaps penetrating the whole MoS<sub>2</sub> thin flake, enabling surface nanogratings to become independent nanoribbons, which was confirmed through SEM (scanning electron microscope), EDX (Energy Dispersive X-ray Detector), and Raman spectra characterization in the work (Figure 2, 3, and 4d).

In order to know how depth of gaps between femtosecond laser induced MoS<sub>2</sub> grating structures can be, experiments on thick MoS<sub>2</sub> film with thickness of micrometer scale was conducted. Through adjusting z-axis angle of SEM sample table, the morphology of periodic-grating structures were observed when sample was tilted 23.2° angle (Figure S2). It indicates that the depth was large than 157/sin23.2°=398.5 nm, which is much larger than the thickness (several to dozens of nanometers) of

MoS<sub>2</sub> flakes used in our work, hence nano-grating structures in the work were independent nanoribbons (Figure S3).

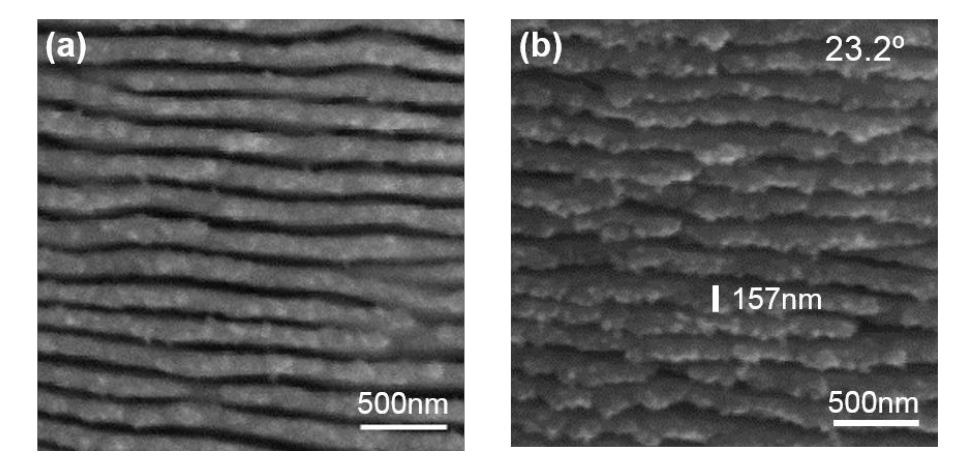


Figure S2. Morphology of periodic-grating structures. (a) No tilt of sample table. (b) Sample table is tilted 23.2°.

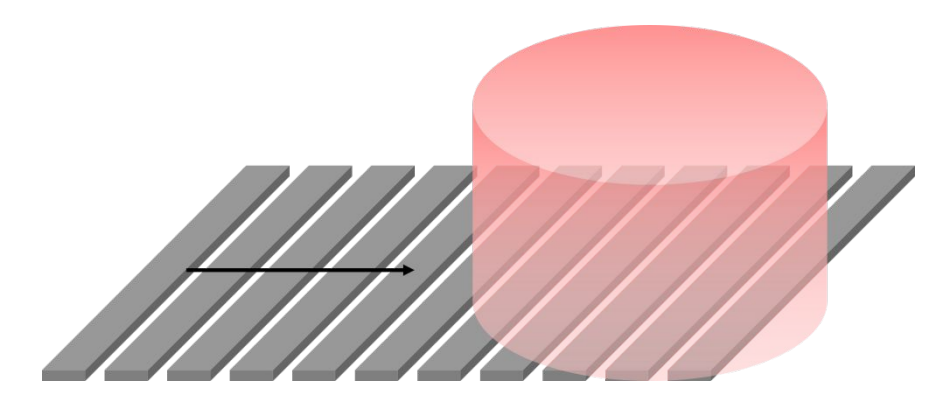


Figure S3. Independent MoS<sub>2</sub> nanoribbons induced by femtosecond laser.

As for the result (singe nanoline with width of 56 nm) shown in the image (above) in Figure 2f. It formed through the material removal at the position of gaps between nanoribbons. The material at gap position collectively ejected out with the appearance of a whole when ablated by femtosecond laser, and then landed on the substrate forming single nanoline.

The different widths of  $MoS_2$  nanoribbons are mainly attributed to the comprehensive effect of laser parameters (pulse energy and scan speed) and thickness

of MoS<sub>2</sub> flakes. MoS<sub>2</sub> nanoribbons with different widths were the good results selected, which were assuredly separated and continuous. For the small size and uncontrollable thickness of mechanically exfoliated MoS<sub>2</sub> flakes, we mainly experimentally analyze the effect of femtosecond laser parameters (pulse energy and scan speed) on the widths of MoS<sub>2</sub> nanostructures. Figure S4 shows the MoS<sub>2</sub> nanostructures processed by femtosecond laser with different pulse energy, indicating that the widths of nanoribbon decrease with the increase of pulse energy. Figure S5 shows the MoS<sub>2</sub> nanostructures processed by femtosecond laser with different scan speed, indicating that the widths of nanoribbon increase with the increase of scan speed.

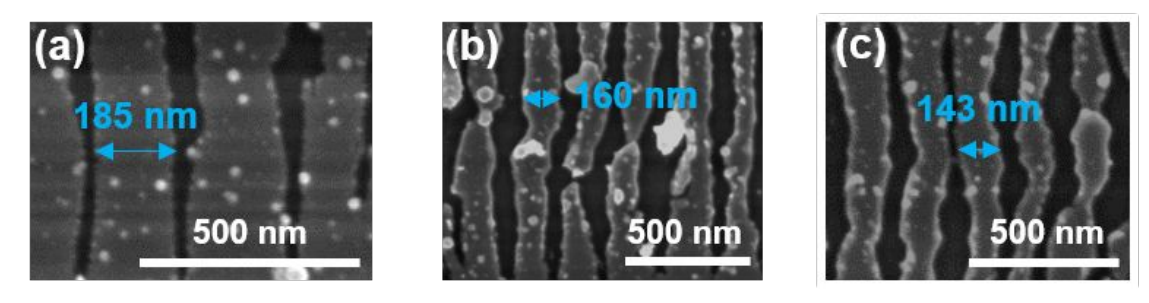


Figure S4.  $MoS_2$  nanostructures processed by femtosecond laser with different pulse energy. (a) 0.015  $\mu$ J, (b) 0.018  $\mu$ J, and (c) 0.021 $\mu$ J (the three experiments were done at the same  $MoS_2$  flake; scan speed was  $20\mu$ m/s).

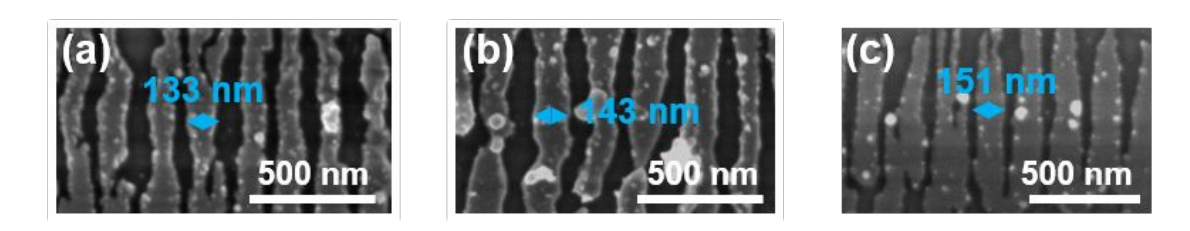


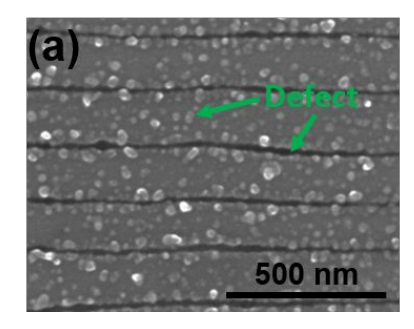
Figure S5. MoS<sub>2</sub> nanostructures processed by femtosecond laser with different scan speed. (a) 20  $\mu$ m/s, (b) 30  $\mu$ m/s, and (c) 50  $\mu$ m/s (the three experiments are doing at the same MoS<sub>2</sub> flake; pulse energy was 0.018  $\mu$ J).

Table S2. Quantitative XPS results for P-MoS<sub>2</sub> and FLP-MoS<sub>2</sub> samples. Corresponding entries are sample number, calculated content of Mo<sup>6+</sup> in Mo, content of O<sub>2</sub> in O, and content of O–Mo in O, according to XPS Mo 3d and O 1s (Figure 4) spectra.

Sample	Content of Mo <sup>6+</sup> in Mo (%)	Content of O <sub>2</sub> in O (%)	Content of O–Mo in O (%)
P-MoS <sub>2</sub>	0	6.70	0
FLP-MoS <sub>2</sub>	13.07	13.36	10.76

### Defects generated by femtosecond laser ablation.

The nanostructured MoS<sub>2</sub> processed by femtosecond laser had rough surfaces with many small debris and long/multilayer edges as shown in Figure S6, hence having many edge-sites at both surface and sides of every nanoribbon. These edges of MoS<sub>2</sub> are defects, which have strong chemical activity contributing to the easily physical and chemical adsorption of oxygen molecules on MoS<sub>2</sub>, S4-5 hence easily achieving obvious p-doping effect on MoS<sub>2</sub>.



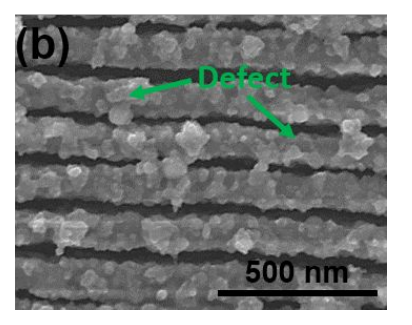


Figure S6. SEM images of two kinds of MoS<sub>2</sub> nanoribbons. It can be seen that there are many MoS<sub>2</sub> debris (with edges) on surface of rough nanoribbons and the long edges of nanoribbons, which were defects.

All-around schematic of the structures of MoS<sub>2</sub> nanoribbons and the source of edge-defects are shown in Figure S7. Figure S7a shows femtosecond laser-processed

MoS<sub>2</sub> nanoribbon array on SiO<sub>2</sub>/Si substrate. Figure S7b, c, and d show the schematic of lattice structure of front, side, and top view of a MoS<sub>2</sub> nanoribbon. Figure S7e shows the schematic of three-dimensional lattice structure of a MoS<sub>2</sub> nanoribbon, indicating the layered-stacked structure of MoS<sub>2</sub>. Every nanoribbon has a few to dozens of layers of MoS<sub>2</sub>, and the four edges of every layer of MoS<sub>2</sub> are edge-defects. In addition, there are many small debris on surface of every nanoribbon, shown as Figure S6 and S7a; Figure S7f shows the schematic of lattice structure of a debris, and the whole edges of debris are defects. In addition, it can be seen that Mo or S atoms at the edges are not completely bonded but unsaturated atoms with dangling bonds, hence have strong chemical activity.<sup>S4-7</sup>

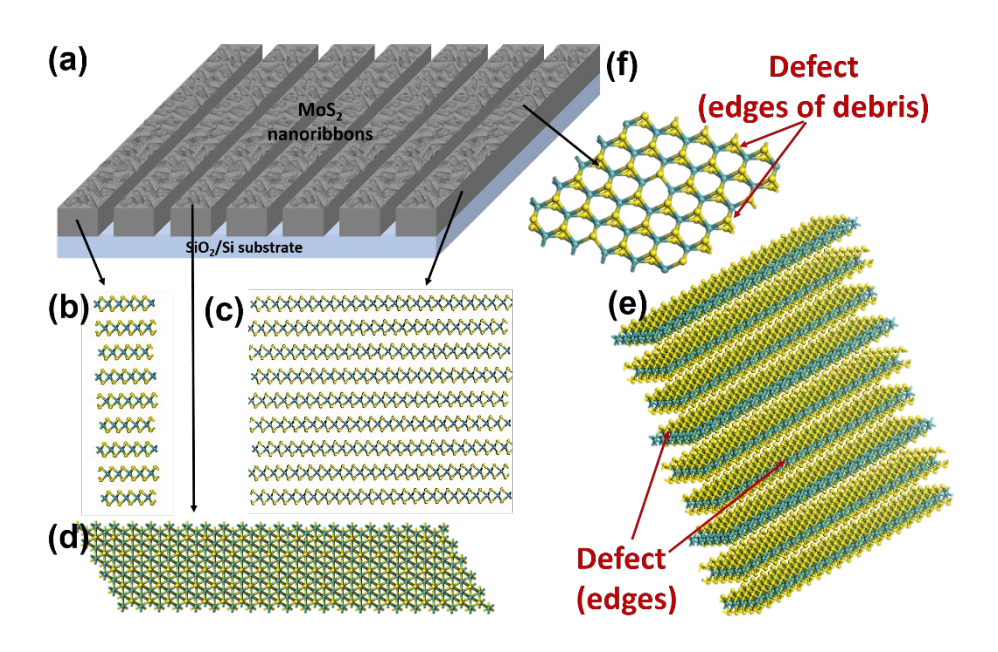


Figure S7. All-around schematic of the structures of MoS<sub>2</sub> nanoribbons and the source of edge-defects. (a) Femtosecond laser-processed MoS<sub>2</sub> nanoribbon array on SiO<sub>2</sub>/Si substrate. Schematic of lattice structures of (b) front, (c) side, and (d) top view of a MoS<sub>2</sub> nanoribbon. (e) Schematic of three-dimensional lattice structure of a MoS<sub>2</sub> nanoribbon. (f) Schematic of lattice structure of a debris.

# Chemical and physical reaction mechanism of laser-processed $MoS_2$ with oxygen molecules.

The oxygen molecules were physically and chemically adsorbed on femtosecond laser-processed MoS<sub>2</sub>. Physical adsorption is attributed to intermolecular forces between adsorbents and adsorbents, also known as van der Waals forces, and cannot form chemical bonds. In the work, chemical adsorption of oxygen molecules on femtosecond laser-processed MoS<sub>2</sub> should be through two process. (1) After MoS<sub>2</sub> surface processed by femtosecond laser, abundant Mo–S bonds (sharing electron pairs) were instantaneously weaken or even broken entirely, S8 leading to dangling bonds and strong chemical activity of Mo and S atoms still staying at sample surface. (2) These active Mo atoms can easily react with oxygen molecules in the air, and chemically combine to be Mo-O bonds. About S, Figure S8 shows the XPS S 2p spectra of pristine (P-) MoS<sub>2</sub> and femtosecond laser-processed (FLP-) MoS<sub>2</sub> flakes. It indicates that the percentage content of S atoms having higher binding energy increased from 24.51% to 33.67%, indicating the increase of binding energy of S atoms after femtosecond laser processing. This indicates that the valence state of S atoms stimulated by femtosecond laser and staying at sample surface became higher. S8 In that way, S atoms stimulated by femtosecond laser but not staying at sample surface should have higher valence state, may have formed gaseous state-S (such as SO or SO<sub>2</sub> molecules), which should spread in the air.

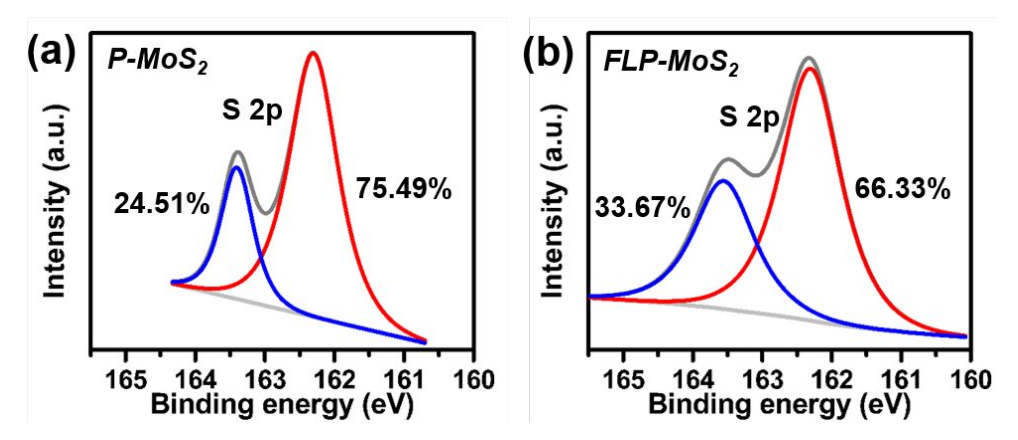


Figure S8. XPS peak-split results of S 2p spectra of (a)  $P-MoS_2$  and (b)  $FLP-MoS_2$ . The detailed percentage contents of S atoms assigned to two peak are calculated through calculating the percentage area of every peak versus the total spectra.

The SO or SO<sub>2</sub> molecules were not detected by XPS according to the XPS O1s and S2p spectra. This may be attributed to following aspects: (1) S atoms of MoS<sub>2</sub> were not that easy to be motivated by femtosecond laser with low energy; (2) activity of S<sup>b-</sup> was not enough to react with O<sub>2</sub> to forming SO or SO<sub>2</sub> molecules; (3) Mo<sup>6+</sup> atoms may be not entirely assigned to MoO<sub>3</sub>, and may also be few MoS<sub>3</sub> (S atoms are still S<sup>2-</sup>) although which is unstable; (4) SO or SO<sub>2</sub> molecules were not easily physically adsorbed and stayed on MoS<sub>2</sub> samples; (5) sensitivity of S atoms is low for XPS detection, and if content of S<sup>2+</sup> and S<sup>4+</sup> from SO or SO<sub>2</sub> molecules was very low, they may be undetectable.

According to above analysis, the chemical reaction of laser-processed  $MoS_2$  with oxygen molecules might be expressed as following:

$$M_o S_2 + h\nu \rightarrow M_o^{a+} + S^{b-} \tag{S1}$$

$$M_O^{a+} + S^{b-} + O_2 \rightarrow M_O O_3 + x M_O S_3 + y S O_2 \uparrow + z S O \uparrow$$
 (S2)

The charge-transfer process of p-doping effect of adsorbed oxygen molecule on FLP-MoS<sub>2</sub> is shown in Figure S9, which can cause the reconfiguration of structural,

electronic and optical characteristics of MoS<sub>2</sub>, and p-doping process can cause a relative shift of Fermi level toward valence band edge.<sup>S9-13</sup>

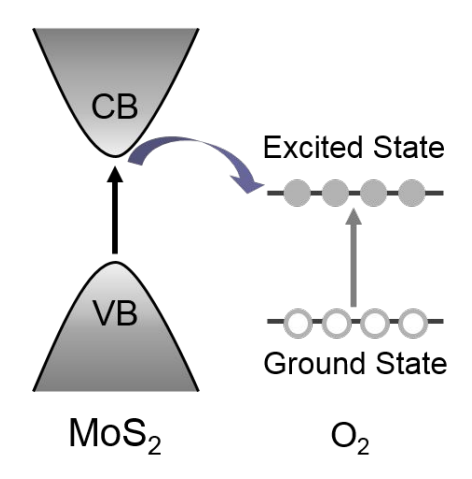


Figure S9. Charge (electron) transfer process between MoS<sub>2</sub> and O<sub>2</sub> (p-doping of O<sub>2</sub> on MoS<sub>2</sub>).

Surface moderate modification of MoS<sub>2</sub> flakes through femtosecond laser pulse processing for FET (-1 and -2). Figure S10 and S11 show the electrical test results for two MoS<sub>2</sub> FET, which are MoS<sub>2</sub> FET-1 and MoS<sub>2</sub> FET-2, before and after surface modified.

Figure S10a and c show the drain-source current ( $I_{DS}$ ) versus drain-source voltage ( $V_{DS}$ ) characteristics of MoS<sub>2</sub> FET-1 before and after surface moderate modification under different gate voltages ( $V_G$ ) ranging from -10 to 10 V. For these output characteristic curve, the drain-source current changed linearly with the drain-source voltage, indicating nearly ohmic contact for these FET device. Figure S10b and d show the drain-source current ( $I_{DS}$ ) versus gate voltages ( $V_G$ ) characteristics of MoS<sub>2</sub> FET-1 before and after surface moderate modification under different drain-source voltage ( $V_{DS}$ ) ranging from 0.05 to 0.5 V. These transfer characteristic curve of pristine/undamaged and surface moderate modified MoS<sub>2</sub> FET exhibited n-type conduction. To further compare the change in electronic properties of

this device, the on/off ratio, carrier mobility (μ), and subthreshold swing (SS) were calculated. For pristine/undamaged MoS<sub>2</sub> FET-1, the on/off ratio, carrier mobility (μ), and SS were respectively 2.84×10<sup>3</sup>, 13.87 cm<sup>2</sup> V<sup>-1</sup> s<sup>-1</sup>, and 14.3 V/dec; for surface modified MoS<sub>2</sub> FET-1, the on/off ratio, carrier mobility (μ), and SS were respectively 1.85×10<sup>5</sup>, 1.55 cm<sup>2</sup> V<sup>-1</sup> s<sup>-1</sup>, and 9.4 V/dec. These results indicated that after femtosecond laser modification processed, the on/off ratio of MoS<sub>2</sub> FET-1 was increased by two magnitude, whereas the carrier mobility was decreased. The increase of on/off ratio might be attributed to the thinning effect of femtosecond laser on MoS<sub>2</sub> flake.<sup>13</sup> And the decrease of carrier mobility might be attributed to the defect states on laser modified-MoS<sub>2</sub>, which can reduce the portion of mobile carriers in conduction band and increase the portion of trapped carriers that do not contribute to charge transport, hence leading to the degradation of effective mobility.<sup>S14</sup>

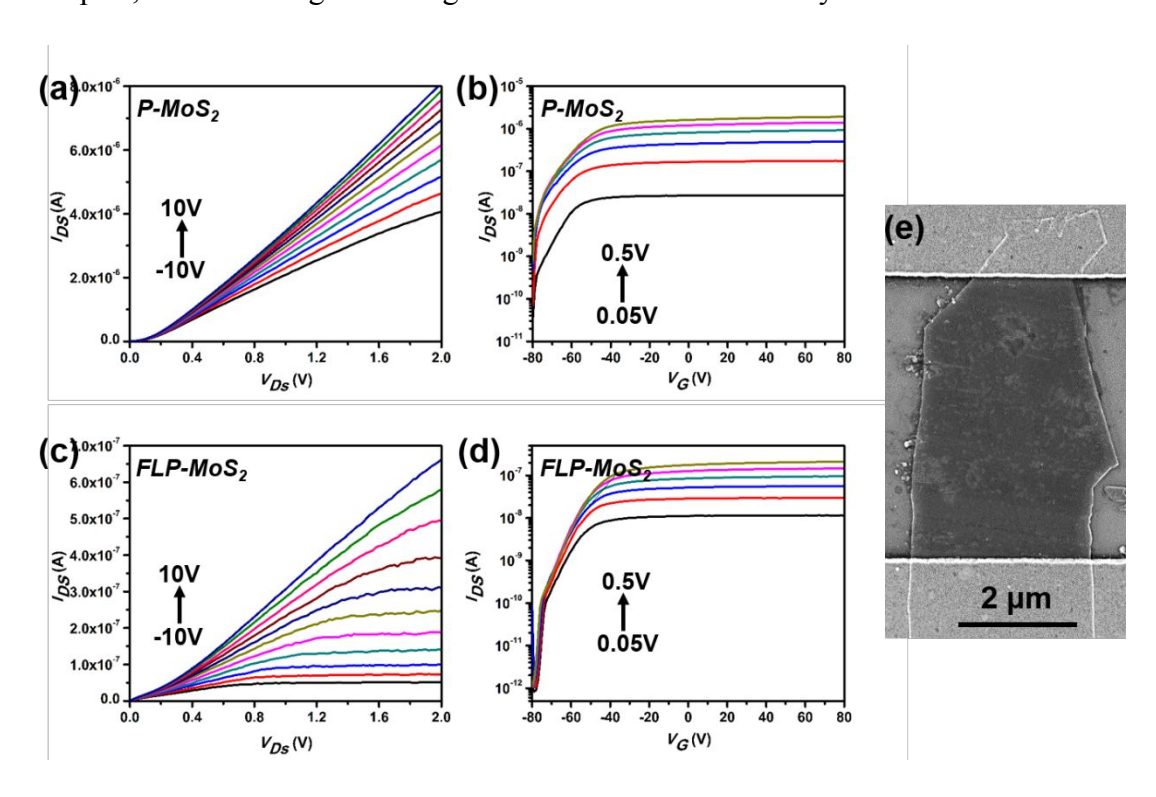


Figure S10. Electrical test of  $MoS_2$  FET-1 before and after surface modification. (a) Output and (b) transfer characteristic curve of  $MoS_2$  FET-1 before surface modification. (c) Output and (d) S-11

transfer characteristic curve of MoS<sub>2</sub> FET-1 after surface modification. (e) SEM image of MoS<sub>2</sub> FET-1 after surface modification.

Figure S11a and c show the drain-source current ( $I_{DS}$ ) versus drain-source voltage  $(V_{DS})$  characteristics of MoS<sub>2</sub> FET-2 before and after surface moderate modification under different gate voltages  $(V_G)$  ranging from -10 to 10 V. For these output characteristic curve, the drain-source current changed linearly with the drain-source voltage, indicating nearly ohmic contact for these FET device. Figure S11b and d show the drain-source current  $(I_{DS})$  versus gate voltages  $(V_G)$ characteristics of MoS<sub>2</sub> FET-2 before and after surface moderate modification under different drain-source voltage  $(V_{DS})$  ranging from 0.75 to 1.5 V. These transfer characteristic curve of pristine/undamaged and surface moderate modified MoS<sub>2</sub> FET exhibited n-type conduction. To further compare the change of electronic properties of this device, the on/off ratio, carrier mobility  $(\mu)$ , and subthreshold swing (SS) were calculated. For pristine/undamaged and surface modified MoS<sub>2</sub> FET-2, the on/off ratio and carrier mobility (µ) were no changed, which were respectively 1.13×10<sup>5</sup> and 3.5×10<sup>-2</sup> cm<sup>2</sup> V<sup>-1</sup> s<sup>-1</sup>, and SS were 18.5 and 11.7 V/dec, respectively. However, the drain-source current ( $I_{DS}$ ) of surface modified MoS<sub>2</sub> FET-2 increased quicker and reached saturation faster with the increase of gate voltages  $(V_G)$  compared with that of pristine/undamaged MoS<sub>2</sub> FET-2.

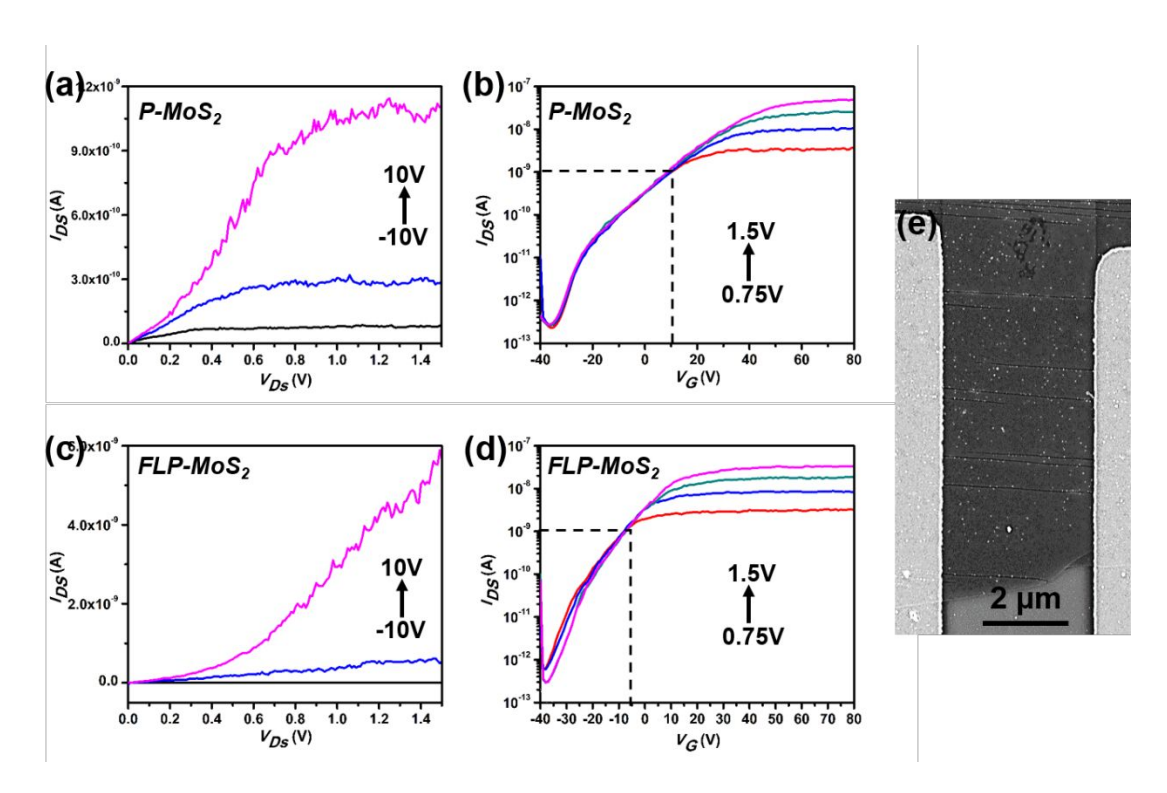


Figure S11. Electrical test of MoS<sub>2</sub> FET-2 before and after surface modification. (a) Output and (b) transfer characteristic curve of MoS<sub>2</sub> FET-2 before surface modification. (c) Output and (d) transfer characteristic curve of MoS<sub>2</sub> FET-2 after surface modification. (e) SEM image of MoS<sub>2</sub> FET-2 after surface modification.

#### Reference

- S1. Shuangshuang, H.; Yanyan, H.; Pingxin, X.; Yi, Z.; Shian, Z.; Tianqing, J.; Zhenrong, S.; Jianrong, Q.; Zhizhan, X., Formation of long- and short-periodic nanoripples on stainless steel irradiated by femtosecond laser pulses. *Journal of Physics D: Applied Physics* **2011**, *44* (50), 505401.
- S2. Xia, B.; Jiang, L.; Li, X.; Yan, X.; Zhao, W.; Lu, Y., High aspect ratio, high-quality microholes in PMMA: a comparison between femtosecond laser drilling in air and in vacuum. *Applied Physics A* **2015**, *119* (1), 61-68.
- S3. Jiang, L.; Wang, A.-D.; Li, B.; Cui, T.-H.; Lu, Y.-F., Electrons dynamics control by shaping femtosecond laser pulses in micro/nanofabrication: modeling, method, measurement and application. *Light: Sci. Appl.* **2018**, *7* (2), 17134.
- S4. Karunadasa, H. I.; Montalvo, E.; Sun, Y.; Majda, M.; Long, J. R.; Chang, C. J., A Molecular MoS<sub&gt;2&lt;/sub&gt; Edge Site Mimic for Catalytic Hydrogen Generation. *Science* **2012**, *335* (6069), 698.
- S5. Jaramillo, T. F.; Jørgensen, K. P.; Bonde, J.; Nielsen, J. H.; Horch, S.; Chorkendorff, I., Identification of Active Edge Sites for Electrochemical H<sub&gt;2&lt;/sub&gt; Evolution from MoS&lt;sub&gt;2&lt;/sub&gt; Nanocatalysts. *Science* **2007**, *317* (5834), 100.
- S6. Voiry, D.; Salehi, M.; Silva, R.; Fujita, T.; Chen, M.; Asefa, T.; Shenoy, V. B.; Eda, G.; Chhowalla, M., Conducting MoS2 Nanosheets as Catalysts for Hydrogen Evolution Reaction. *Nano Letters* **2013**, *13* (12), 6222-6227.
- S7. Li, H.; Tsai, C.; Koh, A. L.; Cai, L.; Contryman, A. W.; Fragapane, A. H.; Zhao, J.; Han, H. S.;

- Manoharan, H. C.; Abild-Pedersen, F.; Nørskov, J. K.; Zheng, X., Activating and optimizing MoS2 basal planes for hydrogen evolution through the formation of strained sulphur vacancies. *Nature Materials* **2015**, *15*, 48.
- S8. Zuo, P.; Jiang, L.; Li, X.; Li, B.; Xu, Y.; Shi, X.; Ran, P.; Ma, T.; Li, D.; Qu, L.; Lu, Y.; Grigoropoulos, C. P., Shape-Controllable Gold Nanoparticle–MoS2 Hybrids Prepared by Tuning Edge-Active Sites and Surface Structures of MoS2 via Temporally Shaped Femtosecond Pulses. *ACS Applied Materials & Interfaces* **2017**, *9* (8), 7447-7455.
- S9. Suh, J.; Tan, T. L.; Zhao, W.; Park, J.; Lin, D.-Y.; Park, T.-E.; Kim, J.; Jin, C.; Saigal, N.; Ghosh, S.; Wong, Z. M.; Chen, Y.; Wang, F.; Walukiewicz, W.; Eda, G.; Wu, J., Reconfiguring crystal and electronic structures of MoS2 by substitutional doping. *Nature Communications* **2018**, *9* (1), 199.
- S10. Fang, H.; Tosun, M.; Seol, G.; Chang, T. C.; Takei, K.; Guo, J.; Javey, A., Degenerate n-Doping of Few-Layer Transition Metal Dichalcogenides by Potassium. *Nano Letters* **2013**, *13* (5), 1991-1995.
- S11. Caballero, A.; Espinós, J. P.; Fernández, A.; Soriano, L.; González-Elipe, A. R., Adsorption and oxidation of K deposited on graphite. *Surface Science* **1996**, *364* (3), 253-265.
- S12. Mahns, B.; Roth, F.; Knupfer, M., Absence of photoemission from the Fermi level in potassium intercalated picene and coronene films: Structure, polaron, or correlation physics? *The Journal of Chemical Physics* **2012**, *136* (13), 134503.
- S13. Chen, M.; Nam, H.; Wi, S.; Ji, L.; Ren, X.; Bian, L.; Lu, S.; Liang, X., Stable few-layer MoS2 rectifying diodes formed by plasma-assisted doping. *Applied Physics Letters* **2013**, *103* (14), 142110.
- S14. Bertolazzi, S.; Bonacchi, S.; Nan, G.; Pershin, A.; Beljonne, D.; Samorì, P., Engineering Chemically Active Defects in Monolayer MoS2 Transistors via Ion-Beam Irradiation and Their Healing via Vapor Deposition of Alkanethiols. *Advanced Materials* **2017**, *29* (18), 1606760.